Nano Research Energy

ISSN 2791-0091 (print); 2790-8119 (online)
https://doi.org/10.26599/NRE.2024.9120125

Research Article

Pre-doped cations in V_2O_5 for high-performance Zn-ion batteries

Yinan Lu[1], Tianlei Wang[2], Nibagani Naresh[1], Joanna Borowiec[2], Ivan P. Parkin[2], and Buddha Deka Boruah[1]

[1] Institute for Materials Discovery, University College London, London WC1E 7JE, UK
[2] Department of Chemistry, University College London, London WC1H 0AJ, UK

Received: 26 January 2024 / **Revised:** 28 April 2024 / **Accepted:** 2 May 2024

ABSTRACT

Aqueous rechargeable zinc-ion batteries (ZIBs) have garnered considerable attention due to their safety, cost-effectiveness, and eco-friendliness. There is a growing interest in finding suitable cathode materials for ZIBs. Layered vanadium oxide has emerged as a promising option due to its ability to store zinc ions with high capacity. However, the advancement of high-performance ZIBs encounters obstacles such as sluggish diffusion of zinc ions resulting from the high energy barrier between V_2O_5 layers, degradation of electrode structure over time and consequently lower capacity than the theoretical value. In this study, we investigated the pre-doping of different cations (including Na^+, K^+, and NH_4^+) into V_2O_5 to enhance the overall charge storage performance. Our findings indicate that the presence of V^{4+} enhances the charge storage performance, while the introduction of NH_4^+ into V_2O_5 (NH_4-V_2O_5) not only increases the interlayer distance ($d_{(001)}$ = 15.99 Å), but also significantly increases the V^{4+}/V^{5+} redox couple (atomic concentration ratio increased from 0.14 to 1.08), resulting in the highest electrochemical performance. The NH_4-V_2O_5 cathode exhibited a high specific capacity (310.8 mAh·g^{-1} at 100 mA·g^{-1}), improved cycling stability, and a significantly reduced charge transfer resistance (~ 17.9 Ω) compared to pristine V_2O_5 (112.5 mAh·g^{-1} at 0.1 A·g^{-1} and ~ 65.58 Ω charge transfer resistance). This study enhances our understanding and contributes to the development of high-capacity cathode materials, offering valuable insights for the design and optimization of cathode materials to enhance the electrochemical performance of ZIBs.

KEYWORDS

pre-doped cations strategy, layered vanadium pentoxide, tuning oxidation states of vanadium, high-charge storage performance, zinc-ion batteries

1 Introduction

The increasing demand for efficient and sustainable energy storage systems has been driven by the rising adoption of renewable energy sources and the urgency to address global warming concerns. While lithium-ion batteries (LIBs) have dominated the market, their limitations such as limited lithium availability, safety issues, and restricted energy density have spurred interest in exploring alternative battery systems [1–4]. Aqueous rechargeable zinc-ion batteries (ZIBs) have emerged as promising candidates due to their abundance, cost-effectiveness, and environmental friendliness. Moreover, their compatibility with aqueous electrolytes offers inherent safety advantages over the flammable organic electrolytes used in traditional LIBs. However, the development of high-performance cathode materials for ZIBs remains a challenging task. Extensive research has focused on manganese oxide [5], Prussian blue analogs [6], vanadium oxide materials [7], and organic compounds [8]. Vanadium oxide-based materials have garnered significant attention due to their high theoretical capacity, multiple oxidation states, and layered structure that facilitates the storage of zinc ions. However, the progress in vanadium cathode development has been impeded by slow ion diffusion, and unstable cycling performance. To address these issues, defect engineering, cation doping, and other approaches have been employed to enhance battery performance [7, 9]. For example, Guo et al. fabricated a layered $K_{0.5}V_2O_5$ with an increased interlayer distance of 9.51 Å, resulting in a boosted capacity of approximately 90 mAh·g^{-1} at 10 mA·g^{-1} [10]. Xu et al. introduced Mg^{2+} doping in V_2O_5, broadening the interlayer distance to 10.76 Å and achieving significantly improved cycling stability with 86.9% capacity retention after 500 cycles [11]. Zheng et al. synthesized Al^{3+} doped hydrated vanadate, attaining a high capacity of 380 mAh·g^{-1} at 50 mA·g^{-1} and maintaining long-term cycling capacity over 3000 cycles [12].

Based on these findings, it is evident that doping cations not only contributes to the stabilization of the crystal structure during cycling but also plays a crucial role in enlarging the interlayer distance, thereby improving the overall capacity. However, the specific functions of different cations in this regard have not been extensively studied. Therefore, the objective of this study was to synthesize and evaluate four types of materials: pristine vanadium

---

Address correspondence to Ivan P. Parkin, i.p.parkin@ucl.ac.uk; Buddha Deka Boruah, b.boruah@ucl.ac.uk

清华大学出版社 Tsinghua University Press | SciOpen

oxide (V_2O_5), sodium-doped vanadium oxide ($Na\text{-}V_2O_5$), potassium-doped vanadium oxide ($K\text{-}V_2O_5$), and ammonium-doped vanadium oxide ($NH_4\text{-}V_2O_5$). Through an analysis of their electrochemical performance, it was observed that $NH_4\text{-}V_2O_5$ exhibited superior performance compared to the other compositions. Notably, the creation of V^{4+}/V^{5+} redox couples, particularly through an increase in the presence of V^{4+}, significantly enhanced the electrochemical performance. These findings provide valuable insights for the future design and development of high-performance cathode materials.

2 Results and discussion

The samples were prepared using chemical routes (see Experimental section) and subsequently processed in hydrothermal reactors. After preparation, their morphology was analyzed using scanning electron microscopy (SEM) and transmission electron microscopy (TEM). Figure 1(a) shows that the pristine V_2O_5 sample has a nanofiber structure with diameters ranging from 20 to 100 nm. The interplanar spacing of 2.208 Å corresponds to the (311) plane according to the reference PDF 03-

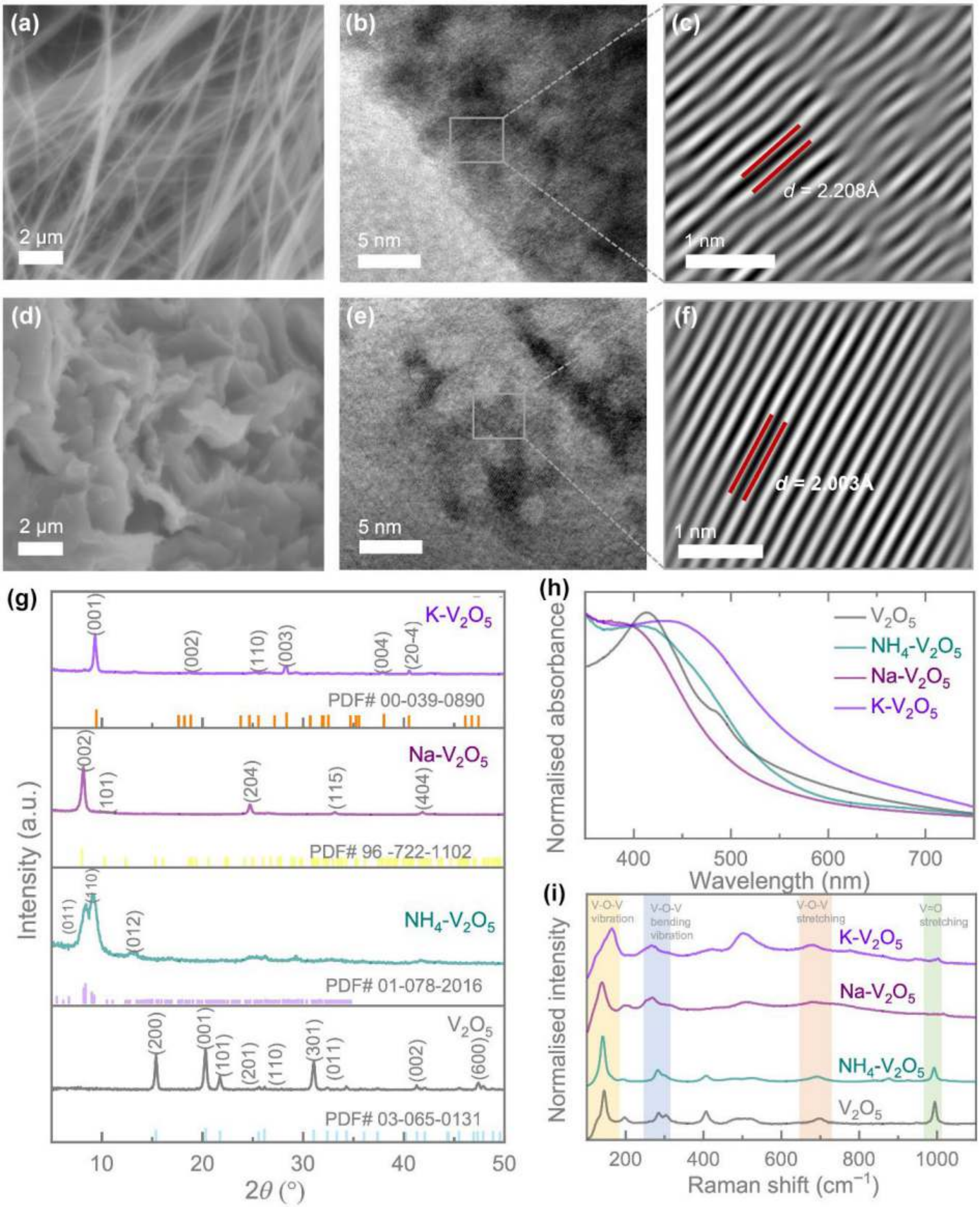

Figure 1 SEM and HRTEM images of V_2O_5 (a–c) and $NH_4\text{-}V_2O_5$ (d–f). (g–i) XRD, UV–Vis and Raman spectra of the V_2O_5, $NH_4\text{-}V_2O_5$, $Na\text{-}V_2O_5$ and $K\text{-}V_2O_5$.

065-0131 (Figs. 1(b) and 1(c)). This observation is supported by the selected area electron diffraction (SAED) results shown in Fig. S1(a) in the Electronic Supplementary Material (ESM). The dots in the SAED pattern correspond to the crystalline planes (201), (301), and (111), with corresponding *d*-spacings of 3.478, 2.925, and 2.673 Å, respectively. On the other hand, the NH_4-V_2O_5 sample exhibits a nanoflakes structure based on the SEM image (Fig. 1(d)). The *d*-spacing calculated from a specific point in the high-resolutionTEM(HRTEM)image(Fig. 1(e))isfoundtobe2.003Å, which corresponds to the X-ray diffraction (XRD) pattern from PDF 01-078-2016. The SAED (Fig. S1(b) in the ESM) analysis further confirms the presence of specific planes, namely $(0\bar{2}1)$, $(0\bar{3}3)$, and $(2\bar{1}4)$, with corresponding *d*-spacings of 6.618, 3.598, and 3.261 Å, respectively. Moreover, the interplanar spacing of V_2O_5 (Fig. S1(c) in the ESM) and NH_4-V_2O_5 (Fig. S1(d) in the ESM) for the (110) plane was measured from HRTEM images. The calculated interplanar spacing values are 3.261 Å for V_2O_5 and 9.55 Å for NH_4-V_2O_5. For the morphologies of Na-V_2O_5 and K-V_2O_5 are not described in the given text but are shown in Figs. S2 and S3 in the ESM. The energy-dispersive X-ray spectroscopy (EDS) images suggest that the cations are uniformly doped in the materials (see Fig. S4 in the ESM). The XRD patterns of the samples correspond to the crystal structures of V_2O_5 (orthorhombic crystal structure with space group *Pmmn* (59)), NH_4-V_2O_5 (anorthic crystal structure with space group $P\bar{1}$), Na-V_2O_5 (orthorhombic crystal structure with space group *Pnma* (62)), and K-V_2O_5 (monoclinic crystal structure with space group *C*12). These XRD patterns are consistent with the SAED and HRTEM patterns (V_2O_5: $a = 11.5120$ Å, $b = 3.5640$ Å, $c = 4.3680$ Å; NH_4-V_2O_5: $a = 13.1730$ Å, $b = 14.3310$ Å, $c = 16.0230$ Å; K-V_2O_5: $a = 11.6570$ Å, $b = 3.6590$ Å, $c = 9.4600$ Å and Na-V_2O_5: $a = 9.3620$ Å, $b = 3.6080$ Å, $c = 22.0580$ Å). To further investigate the optical properties of the samples, the UV–Vis absorption spectrum is explored and presented in Fig. 1(h). It is observed that there are significant changes in the optical absorption properties among the samples. The calculated optical bandgap energies for V_2O_5, NH_4-V_2O_5, Na-V_2O_5, and K-V_2O_5 samples are ~2.5, ~2.3, ~2.4, and ~ 2.0 eV, respectively (see Fig S5 in the ESM). The shift in ultraviolet (UV) peaks is caused by lattice expansion and the formation of oxygen vacancies due to pre-doping with cations. In certain materials, the spacing between layers can affect the electronic band structure, thereby influencing the absorption or emission of light, including UV light. This means that the interlayer spacing plays a crucial role in determining optical properties. Alterations in this interlayer gap, through methods like pressure, strain, or chemical doping, can change the energy levels associated with electronic transitions, leading to shifts in UV absorption or emission peaks. Moreover, Fig. 1(i) shows Raman spectra that exhibit characteristic shifts that can be assigned as follows the peak centered around ~993 cm^{-1} corresponds to the stretching vibration of the vanadyl bond (V=O). The peak at ~700 cm^{-1} is associated with the stretching of V-O-V bonds. The peak located at ~526 cm^{-1} corresponds to the V_3O phonon band. The peak at ~404 cm^{-1} represents the angle-bending vibration of V-$O_{(3)}$-V. The peak at ~304 cm^{-1} corresponds to the bending vibration of V-O_C. The peak at ~284 cm^{-1} corresponds to the bond bending vibration of O_C-V-O_B. The peak at ~197 cm^{-1} represents the bending vibration of O_C-V-O_B (A_g mode) bond. Finally, the peak at ~145 cm^{-1} corresponds to the vibration mode of V-O-V chains [13]. For NH_4-V_2O_5, the peaks centered around ~142 and ~283 cm^{-1} are assigned to the bending vibration of O-V=O. The peaks at ~194, ~301, and ~ 405, and 476 cm^{-1} are attributed to the bending vibration of V-O-V. The peaks at ~692 cm^{-1} is associated to the stretching vibration of the V-O bond [14]. The peak at ~993 cm^{-1} is ascribed to the symmetric stretching vibration of V=O. For Na-V_2O_5, the peak at ~137 cm^{-1} is assigned to the vibration mode of V-O-V chains with a blueshift. The peak at at ~200 cm^{-1} is associated with the bending vibration with a red shift. The peak ~692 cm^{-1} mode corresponds to the antisymmetric stretching of $V_{(1)}$–$O_{(2)}$–$V_{(1)}$ and the mode at ~1014 cm^{-1} represents the $V_{(2)}$–$O_{(6)}$ stretching vibration [15]. For K-V_2O_5, the characteristic peak ~1014 cm^{-1} is ascribed to the V=O stretching modes in the δ-phase. The peaks at ~500 and ~686 cm^{-1} are assigned to the stretching modes of the V-O bonds. The peaks at 416 cm^{-1} is correspond to the V=O bending vibration [10].

To gain a better understanding of the formulation and oxidation states of vanadium in the samples, we conducted an X-ray photoelectron spectroscopy (XPS) investigation. In Fig. 2(a), the O 1s spectrum appears broad and asymmetric, allowing for its deconvolution into three peaks. These peaks indicate the presence of three different oxygen species. The peaks are located at approximately ~529.95 eV (fitted orange peak), ~531.00 eV (fitted red peak), and ~532.40 eV (fitted yellow peak). The peaks correspond to which correspond to the lattice oxygen O^{2-}, the absorbed H_2O molecules and, oxygen vacancy, respectively [16]. Notably, the peaks related to the presence of H_2O molecules and oxygen vacancy exhibit a noticeable increase in intensity in NH_4-V_2O_5 compared to V_2O_5, following the order: absorbed H_2O molecules Na-V_2O_5 (10.25%) > NH_4-V_2O_5 (9.13%) > K-V_2O_5 (7.5%) > V_2O_5 (7.07%); oxygen vacancy from NH_4-V_2O_5 (6.31%) > K-V_2O_5 (2.76%) > V_2O_5 (2.24%) > Na-V_2O_5 (2.14%). Figure 2(b) illustrates the core level binding energies of the V $2p_{3/2}$ and V $2p_{1/2}$ spectra, which can be divided into four peaks at approximately ~517.16 and 524.51 eV (fitted light blue) peaks attributed due to the presence of pentavalent state (V^{5+}), whereas ~523.10 and ~515.76 eV (fitted light green) which correspond to the tetravalent vanadium (V^{4+}). The ratio of V^{4+}:V^{5+} increases in the doped samples, following the order NH_4-V_2O_5 (1.08) > K-V_2O_5 (0.99) > Na-V_2O_5 (0.83) > V_2O_5 (0.14) (Fig. S1 in the ESM). This indicates an increase in the presence of V^{4+} after doping compared to the pristine V_2O_5 sample. Among the doped samples, NH_4-V_2O_5 exhibits the highest value of V^{4+}. Figure 2(c) presents the thermogravimetric analysis (TGA) curves of the samples. The weight losses of 1.87% (V_2O_5), 8.41% (NH_4-V_2O_5), 10.16% (Na-V_2O_5), and 2.80% (K-V_2O_5) observed in the temperature range of 55–200 °C are attributed to the removal of adsorbed and constitutional water molecules. The order of water molecule content, as indicated in Fig. 2(a), aligns with the XPS results.

Next, the electrochemical performance of the electrodes was thoroughly investigated against a zinc (Zn) anode by assembling coin cells according to the experimental procedure outlined in the experimental section. To assess the performance, the first cyclic voltammogram (CV) was conducted across a range of scan rates from 0.2 to 1.0 $mV·s^{-1}$, covering a potential window of 0.2 to 1.6 V. Figure 3(a) depicts the CVs of the V_2O_5 electrode, showcasing distinct pairs of oxidation and reduction peaks. These peaks are observed around specific voltage values, such as major peaks (~1.2 V / ~0.9 V) and minor peaks (~0.7 V / ~0.5 V), which are attributed to the intercalation and de-intercalation processes of Zn^{2+} ions [17, 18]. The CVs of NH_4-V_2O_5, on the other hand, exhibit pronounced oxidation and reduction peaks with significantly higher specific peak currents when compared to pristine V_2O_5. This enhanced performance suggests an improved capability for charge storage in NH_4-V_2O_5. For a comprehensive

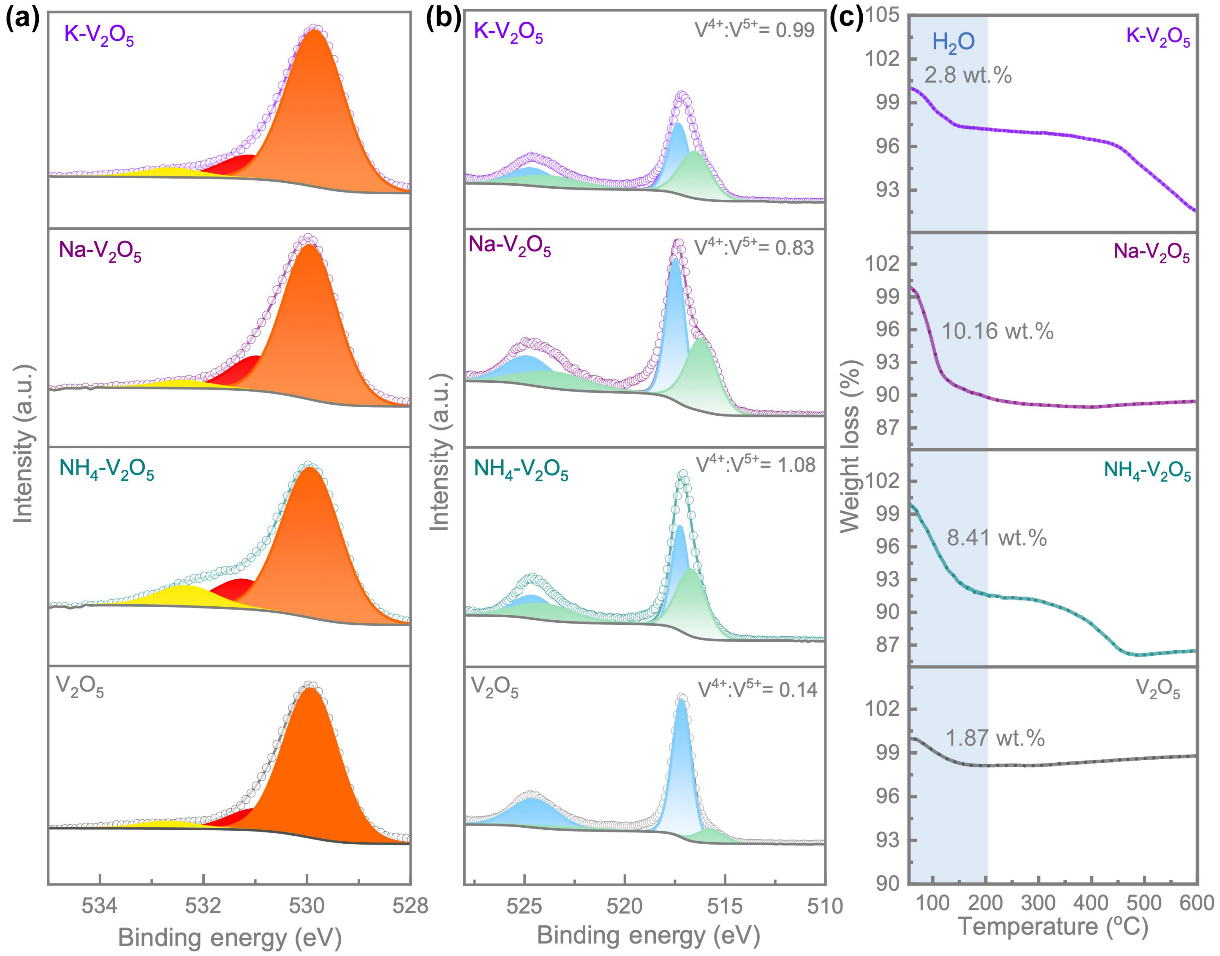

Figure 2 XPS spectra of the samples: (a) O 1s and (b) V $2p_{1/2}$ and V $2p_{3/2}$. (c) TGA curves of the of the samples.

analysis, the CVs of Na-V_2O_5 and K-V_2O_5 can be found in the Supporting Information (Figs. S6 and S7 in the ESM). It is noteworthy that all the doped electrodes display enhanced charge storage capabilities compared to the pristine V_2O_5 electrodes. Notably, NH_4-V_2O_5 electrodes demonstrate the highest response among the doped samples. Furthermore, when comparing the CVs at 0.5 and 1.0 mV·s^{-1}, it becomes evident that the redox peak currents are substantially improved, indicating a significant enhancement in charge storage activities across the doped electrodes. Overall, these findings highlight the superior electrochemical performance of the doped electrodes, with NH_4-V_2O_5 exhibiting the most notable improvements.

Moreover, Table S2 in the ESM demonstrates the *b*-values calculation for the cathodic and anodic peaks [19, 20]. For the CV curves of pristine V_2O_5, the *b*-values for the cathodic and anodic peaks are 0.79 and 0.56, respectively. Similarly, for NH_4-V_2O_5 CV curves, the calculated *b*-values for the two cathodic peaks are 0.66 and 0.85, while the *b*-values for the anodic peaks are 0.74 and 0.73, respectively. In both the V_2O_5 and NH_4-V_2O_5 samples, the *b*-values exceed 0.5, indicating that the electrochemical behavior of the electrodes is a combination of capacitive and diffusion-controlled mechanisms, with capacitive control being more dominant. To analyze the charge storage process, we can break it down into two components: capacitive-controlled ($k_1 v$) and diffusion-controlled ($k_2 v^{1/2}$). This relationship can be represented by the current at a fixed voltage equation: $i(V) = k_1 v + k_2 v^{1/2}$ [19, 20]. Using this equation, we calculated the capacitive contribution, as shown in Figs. 3(e) and 3(f), Figs. S6(b) and S7(b) in the ESM, for different electrodes. At a scan rate of 0.2 mV·s^{-1}, the estimated capacitive contributions for V_2O_5, NH_4-V_2O_5, Na-V_2O_5, and K-V_2O_5 electrodes were 55.40%, 58.7%, 65%, and 39.7%, respectively. These values increased to 75.5%, 75.7%, 80.5%, and 59.4% when tested at 1.0 mV·s^{-1}. A higher capacitive profile indicates a better ability to operate batteries at high rates. Therefore, among all the electrodes, NH_4-V_2O_5 and Na-V_2O_5 electrodes appear to be more suitable for high-rate operation (see further). Furthermore, NH_4-V_2O_5 demonstrates superior charge storage performance even at lower rates (for more information, please see the accompanying details).

The charge storage analysis of the electrodes was further extended by evaluating the galvanostatic discharge-charge (GDC) response at different specific currents, ranging from 100 mA·g^{-1} to 5000 mA·g^{-1}, across the working potential range of 0.2 to 1.6 V. Detailed GDC curves for V_2O_5 and NH_4-V_2O_5 at various specific currents are shown in Figs. 4(a) and 4(b), respectively. Consistent with the CV results, NH_4-V_2O_5 demonstrated higher specific capacities compared to the other electrodes. For example, at a specific current of 100 mA·g^{-1}, the observed specific capacities (2nd cycle) were 99.6, 302.4, 238.17, and 276 mAh·g^{-1} for V_2O_5, NH_4-V_2O_5, Na-V_2O_5, and K-V_2O_5 electrodes, respectively. Figures 4(c) and 4(d) clearly illustrate the capacity improvements in the doped samples compared to pristine V_2O_5. However, at a high specific current of 5000 mA·g^{-1}, the specific capacities of NH_4-V_2O_5 and Na-V_2O_5 were nearly equal (159 mAh·g^{-1}). This similarity could be attributed to the higher capacitive-controlled charge storage contribution, which dominates at relatively higher rates. Figure S8

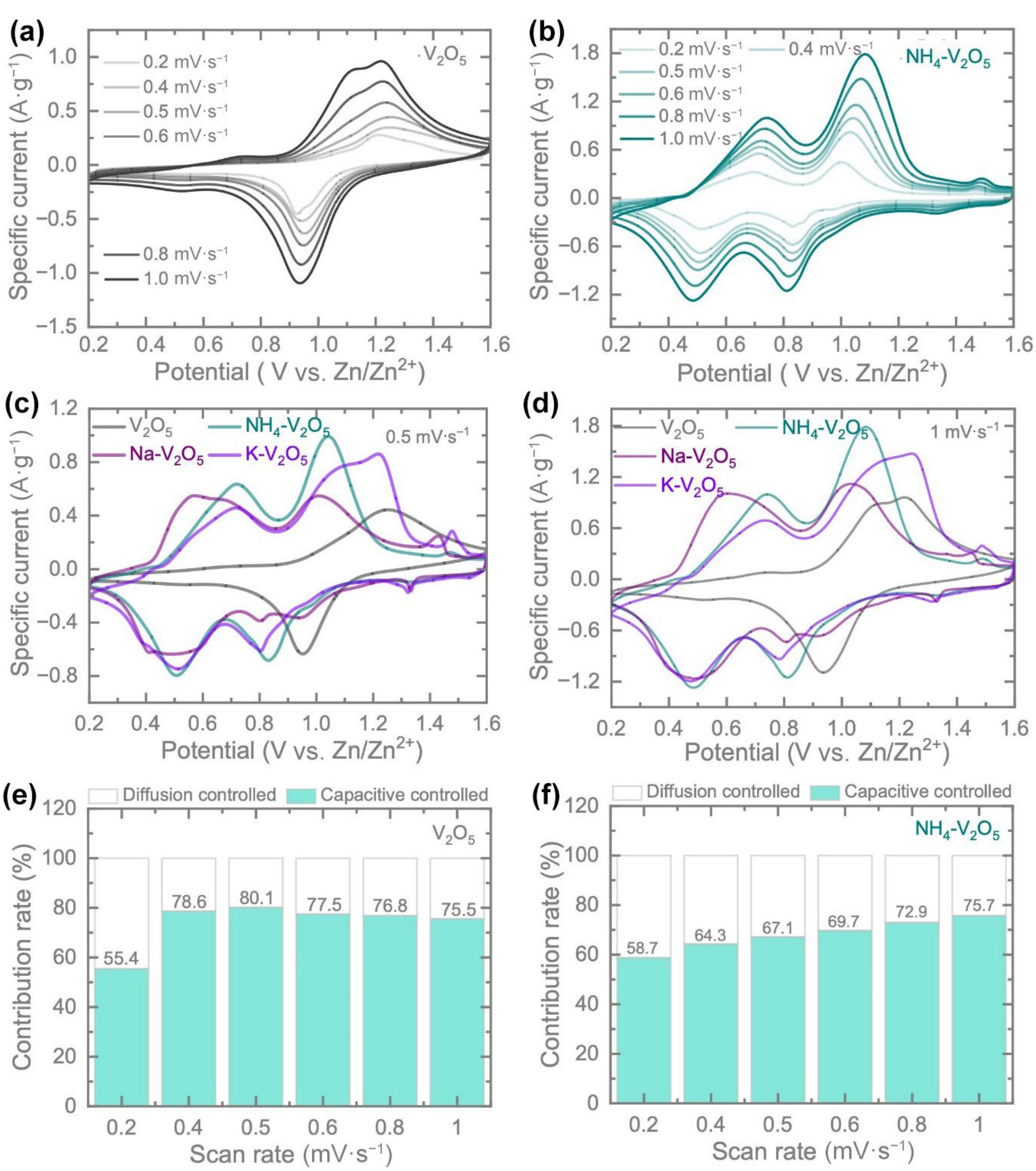

Figure 3 CV curves of (a) V_2O_5 and (b) NH_4-V_2O_5 obtained at various scan rates ranging from 0.2 to 1.0 mV·s^{-1} within a voltage window of 0.2 to 1.6 V. Comparison of the CVs of the samples at scan rates of (c) 0.5 mV·s^{-1} and (d) 1.0 mV·s^{-1}. Estimation of the charge storage contribution for (e) V_2O_5 and (f) NH_4-V_2O_5 electrodes.

in the ESM provides additional GDC curves for Na-V_2O_5 and K-V_2O_5 electrodes. The observed capacity improvements in the electrodes closely follow the presence of V^{4+}:V^{5+} states (Fig. 2(b), Table S1 in the ESM), following the sequence V_2O_5 < Na-V_2O_5 < K-V_2O_5 < NH_4-V_2O_5. This sequential order directly corresponds to the charge storage performance. Therefore, the highest capacity observed in NH_4-V_2O_5 compared to the other electrodes can primarily be attributed to the higher concentration of V^{4+}, which is more efficient for reversible Zn^{2+} storage [21–23].

In addition to GDC tests, electrochemical impedance spectroscopy (EIS) tests were conducted within a frequency range of 10 mHz to 100 kHz with a voltage amplitude of 10 mV. These tests were performed after the 2nd GDC cycle to 0.7 V. The Nyquist plots in Fig. S9 in the ESM revealed the charge transfer resistances of the cells, which were measured to be approximately 65.58 Ω for V_2O_5, 17.9 Ω for NH_4-V_2O_5, 19.78 Ω for Na-V_2O_5, and 10.66 Ω for K-V_2O_5 cells. These results further confirm that the doped samples exhibit better charge storage kinetics compared to the pristine counterpart. Furthermore, long-term cycling tests at 1000 mA·g^{-1} for 1000 cycles were conducted, as depicted in Fig. 4(a) for NH_4-V_2O_5, a capacity retention of approximately 60.58% and a Coulombic efficiency (CE) of 100% were achieved after 1000 cycles. Additionally, Fig. S10 in the ESM displays the *ex-situ* HRTEM image and the interplanar spacing (*d*-value) for NH_4-V_2O_5 after 500 cycles. The calculated (110) *d*-spacing for NH_4-V_2O_5 after 500 cycles is 9.65 Å, which is slightly larger than the pre-cycling value of 9.55 Å. Furthermore, Table S3 in the ESM compares the electrochemical performance of NH_4-V_2O_5 with reported studies on V_2O_5, indicating that our material exhibits promising charge storage capabilities.

In conclusion, this study focused on the investigation of pre-doping of various cations, including Na^+, K^+ and NH_4^+ into V_2O_5

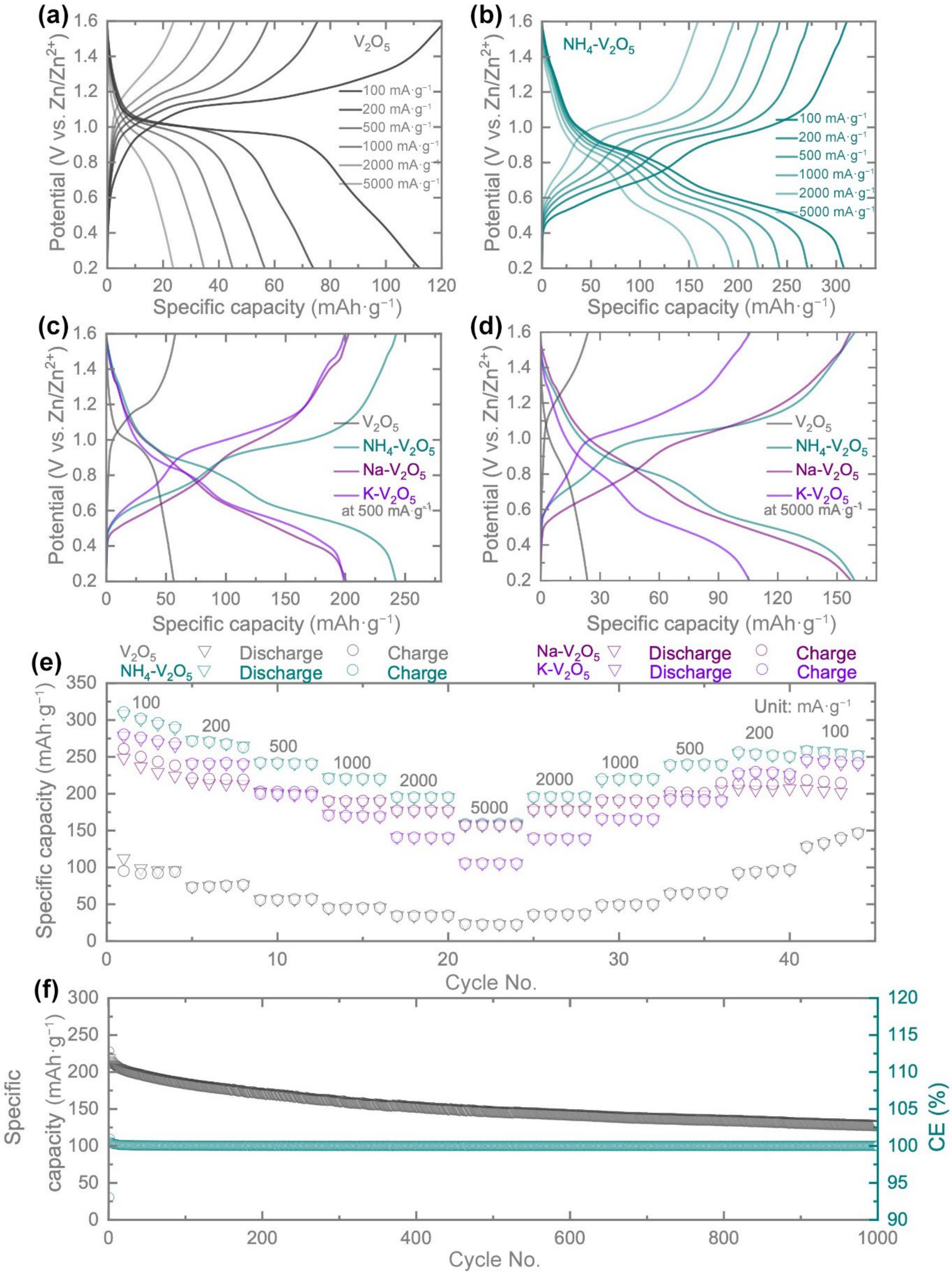

Figure 4 (a) and (b) GDC curves of V_2O_5 and NH_4-V_2O_5 at various specific currents, spanning from 100 to 5000 mA·g^{-1}, across the voltage range of 0.2 to 1.4 V. (c) and (d) Comparative GDC curves of the electrodes at specific currents of 500 and 5000 mA·g^{-1}, respectively. (e) Rate tests showcasing the performance of the electrodes. (f) Long-term cycling test of NH_4-V_2O_5, where CE represents Coulombic efficiency in the plot.

to enhance the overall charge storage performance of ZIBs. Our findings highlight the crucial role played by V^{4+} species in enhancing the cathode material's charge storage performance. Additionally, the introduction of NH_4^+ into V_2O_5, resulting in NH_4-V_2O_5, led to notable improvements. One significant improvement observed was the increase in interlayer distance to 15.99 Å ($d_{(001)}$ = 15.99 Å), which promotes efficient diffusion of Zn ions within the material. Moreover, the increase in V^{4+}/V^{5+} redox couple ratio from 0.14 to 1.08 demonstrates enhanced electrochemical performance. The NH_4-V_2O_5 cathode exhibited a high specific capacity of 310.8 mAh·g^{-1} at 100 mA·g^{-1}, indicating its ability to store a substantial amount of charge with improved cycling stability. By advancing our understanding of the doping process and the role of different cations in V_2O_5, this study provides valuable insights for the design and optimization of cathode materials in ZIBs. These insights contribute to the ongoing efforts to develop more efficient and reliable rechargeable battery systems, ultimately enhancing the charge storage performance and overall sustainability of ZIB technology.

3 Experimental section

Chemicals: All chemicals in the study were of analytical grade and used directly without any further purification. Vanadium pentoxide, hydrogen peroxide solution 30% (*w*/*w*), ammounium metavanadate, potassium iodide, polyethylene glycol (M_W=4000), sulfuric acid (95%–97%), $Zn(CF_3SO_3)_2$, ethanol and poly(vinyl difluoride) were received from Sigma-Aldrich. N-methyl-2-pyrrolidone technical was purchased from VWR international. Sodium hydroxide pellets, 98% was purchased from thermo scientific. Potassium chloride was received from EMSURE®. Reduced graphene oxide powder (rGO), P_3HT (M_W=60,150 97.6% RR) were purchased from Ossila.

Material synthesis: Pristine V_2O_5 was synthesized using a hydrothermal process. In this process, 1.0930 g of V_2O_5 powder was added to 90 mL of deionized (DI) water, and the solution was vigorously stirred at around 300 rpm for 30 min at room temperature. Following that, 15 mL of 30% H_2O_2 was added to the solution, and stirring continued for an additional 30 min. The resulting transparent orange solution was then transferred into a 150 mL autoclave and placed in an oven at 205 °C for 3 days. Once cooled to room temperature, the products were washed alternately with DI water and ethanol and finally dried in a vacuum oven overnight at 70 °C.

The synthesis of NH_4-V_2O_5 was conducted following the method described in Ref. [14]. In this procedure, 1.755 g of ammonium metavanadate was added to 90 mL of DI water. The solution was stirred for 30 min before adding 0.9 mL of H_2SO_4 to the suspension. Stirring was continued for an additional 30 min. The resulting suspension was then transferred to a 150 mL autoclave and placed in an oven at 100 °C for 2 days. After cooling to room temperature, the products were washed alternately with DI water and ethanol and dried in a vacuum oven overnight at 70 °C.

The synthesis of Na-V_2O_5 followed the method described in Ref. [15]. Initially, 0.3636 g of pristine V_2O_5 was dissolved in a mixture of 60 mL of DI water and 0.7 mL of NaOH solution (1 mol·L^{-1}). The solution was sonicated at room temperature for 1 hour. Subsequently, 0.2 g of Polyethylene glycol (M_W=4000) was added to the solution, and stirring was continued for another 15 min. The solution was then transferred to a 150 mL autoclave and placed in an oven at 180 °C for 2 days. After cooling to room temperature, the products were washed alternately with DI water and ethanol and dried in a vacuum oven overnight at 70 °C.

The fabrication of K-V_2O_5 followed the procedure described in Ref. [10]. In this process, 0.5456 g of pristine 0.747 g of KI, and 6.709 g of KCl were dissolved in 90 mL of DI water with magnetic stirring for 30 min. The solution was transferred to a 150 mL autoclave and placed in an oven at 200 °C for 1 day. After cooling to room temperature, the products were washed alternately with DI water and ethanol and dried in a vacuum oven overnight at 70 °C.

Characterization: The obtained materials underwent characterization using various analytical methods. SEM analysis was conducted using a Zeiss EVO LS15, Oxford Instruments X-MaxN, and Hitachi TMA4000Plus. TEM, EDS, and SAED were performed using a JEOL JEM-2100 TEM operated at 200 kV. XRD patterns of the samples were obtained using the Panalytical Empyrean XRD instrument with Cu Kα radiation. The measurements were conducted at 40 kV and 40 mA, with a step size of 0.05° and a scanning rate of 0.1 °·s^{-1}, covering a 2θ range from 2° to 70°. UV–Vis analysis was carried out using the PerkinElmer Lambda 750S instrument. Raman spectroscopy was performed using the Renishaw inViaTM confocal Raman microscope with a laser wavelength of 515 nm. XPS analysis was conducted using the ThermoFisher Scientific XPS instrument. The XPS data were acquired using monochromatic Al Kα X-rays (1486.6 eV), with a pass energy of 50 and 200 eV for narrow and wide spectra, respectively. No significant sample charging was observed, and charge referencing was done against adventitious carbon (C 1s, 284.8 eV). The spectra are presented with intensity in counts per second (CPS), and the experimental peaks were fitted using CasaXPS software.

Preparation of cathodes and coin-cells: To prepare the cathodes, 80 mg of active material, consisting of either V_2O_5, NH_4-V_2O_5, Na-V_2O_5, or K-V_2O_5, along with 10 mg of rGO and 5 mg of P_3HT, was dispersed in 2 mL of NMP through a sonication process. Subsequently, 5 mg of PVDF (polyvinylidene fluoride) was added to the solution. The resulting electrode solution was drop-cast onto CF (Sigracet GDL 39 AA carbon graphite paper, SGL Carbon) current collectors and dried under vacuum conditions at 70 °C, resulting in the formation of the cathodes. The CR 2032 coin-cells were assembled by placing a titanium foil on the coin-cell case, followed by the placement of a cathode disc. A Whatman glass microfiber filter paper was then placed as a separator. Next, 150 μL of a 3 M $Zn(CF_3SO_3)_2$ aqueous electrolyte was added to the cell, and finally, a Zn counter electrode was introduced in sequence.

Electrochemical tests: CV measurements were carried out using a Biologic VMP-3 galvanostat, covering a potential window of 0.2 to 1.6 V after resting the cells for 10 hours. The measurements were conducted at various scan rates ranging from 0.2 to 1.0 mV·s^{-1}. GDC measurements were performed over the same potential window at different specific currents, ranging from 100 to 5000 mA·g^{-1}. The cycling performance of the electrodes was evaluated by testing them using Neware (BTS4000) at a constant current of 1000 mA·g^{-1} for 1000 cycles, maintaining the same potential window. EIS tests (Autolab, PGSTAT302N) were conducted within a frequency range of 10 mHz to 100 kHz, using a voltage amplitude of 10 mV.

Electronic Supplementary Material: Supplementary material (SAED patterns and HETEM images (Fig. S1); SEM, TEM, HRTEM images and SAED patterns (Figs. S2 and S3); Computed V^{4+} and V^{5+} values (Table S1); EDS mappings (Fig. S4); Tauc plots (Fig. S5); CVs and estimation of the charge storage contribution (Figs. S6 and S7); GCDs of Na-V_2O_5 and K-V_2O_5 (Fig. S8); Nyquist plots and equivalent circuit model (Fig. S9); *b*-values calculations (Table S2); HRTEM image of cycled electrode (Fig. S10); specific capacities comparision table (Table S3)) is available in the online version of this article at https://doi.org/10.26599/NRE.2024.9120125.

Declaration of conflicting interests

The authors declare no conflicting interests regarding the content of this article.

Data availability

All data needed to support the conclusions in the paper are presented in the manuscript and/or the Supplementary Materials. Additional data related to this paper may be requested from the corresponding author upon request.

References

[1] Mahmood, N.; Tang, T. Y.; Hou, Y. L. Nanostructured anode materials for lithium ion batteries: Progress, challenge and perspective. *Adv. Energy Mater.* **2016**, *6*, 1600374.

[2] Passerini, S.; Scrosati, B. Lithium and lithium-ion batteries: Challenges and prospects. *Electrochem. Soc. Interface* **2016**, *25*, 85–87.

[3] Huang, Q. K.; Ni, S. Y.; Jiao, M. L.; Zhong, X. W.; Zhou, G. M.; Cheng, H. M. Aligned carbon-based electrodes for fast-charging batteries: A review. *Small* **2021**, *17*, 2007676.

[4] Diouf, B.; Pode, R. Potential of lithium-ion batteries in renewable energy. *Renew. Energy* **2015**, *76*, 375–380.

[5] Chen, Q.; Jin, J. L.; Kou, Z. K.; Liao, C.; Liu, Z. A.; Zhou, L.; Wang, J.; Mai, L. Zn^{2+} pre-intercalation stabilizes the tunnel structure of MnO_2 nanowires and enables zinc-ion hybrid supercapacitor of battery-level energy density. *Small* **2020**, *16*, 2000091.

[6] Zhang, L. Y.; Chen, L.; Zhou, X. F.; Liu, Z. P. Towards high-voltage aqueous metal-ion batteries beyond 1.5 V: The zinc/zinc hexacyanoferrate system. *Adv. Energy Mater.* **2015**, *5*, 1400930.

[7] Chen, H. L.; Cheng, S. L.; Chen, D.; Jiang, Y.; Ang, E. H.; Liu, W. L.; Feng, Y. Z.; Rui, X. H.; Yu, Y. Vanadate-based electrodes for rechargeable batteries. *Mater. Chem. Front.* **2021**, *5*, 1585–1609.

[8] Han, C. P.; Li, H. F.; Shi, R. Y.; Zhang, T. F.; Tong, J.; Li, J. Q.; Li, B. H. Organic quinones towards advanced electrochemical energy storage: Recent advances and challenges. *J. Mater. Chem. A* **2019**, *7*, 23378–23415.

[9] Zhu, K. F.; Wei, S. Q.; Shou, H. W.; Shen, F. R.; Chen, S. M.; Zhang, P. J.; Wang, C. D.; Cao, Y. Y.; Guo, X.; Luo, M. et al. Defect engineering on V_2O_3 cathode for long-cycling aqueous zinc metal batteries. *Nat. Commun.* **2021**, *12*, 6878.

[10] Deng, L. Q.; Niu, X. G.; Ma, G. S.; Yang, Z.; Zeng, L.; Zhu, Y. J.; Guo, L. Layered potassium vanadate $K_{0.5}V_2O_5$ as a cathode material for nonaqueous potassium ion batteries. *Adv. Funct. Mater.* **2018**, *28*, 1800670.

[11] Xu, X. M.; Duan, M. Y.; Yue, Y. F.; Li, Q.; Zhang, X.; Wu, L.; Wu, P. J.; Song, B.; Mai, L. Bilayered $Mg_{0.25}V_2O_5 \cdot H_2O$ as a stable cathode for rechargeable Ca-ion batteries. *ACS Energy Lett.* **2019**, *4*, 1328–1335.

[12] Zheng, J. Q.; Liu, C. F.; Tian, M.; Jia, X. X.; Jahrman, E. P.; Seidler, G. T.; Zhang, S. Q.; Liu, Y. Y.; Zhang, Y. F.; Meng, C. G. et al. Fast and reversible zinc ion intercalation in Al-ion modified hydrated vanadate. *Nano Energy* **2020**, *70*, 104519.

[13] Boruah, B. D.; Wen, B.; De Volder, M. Light rechargeable lithium-ion batteries using V_2O_5 cathodes. *Nano Lett.* **2021**, *21*, 3527–3532.

[14] Xu, L.; Zhang, Y.; Zheng, J.; Jiang, H.; Hu, T.; Meng, C. Ammonium ion intercalated hydrated vanadium pentoxide for advanced aqueous rechargeable Zn-ion batteries. *Mater. Today Energy* **2020**, *18*, 100509.

[15] He, P.; Zhang, G. B.; Liao, X. B.; Yan, M. Y.; Xu, X.; An, Q. Y.; Liu, J.; Mai, L. Sodium ion stabilized vanadium oxide nanowire cathode for high-performance zinc-ion batteries. *Adv. Energy Mater.* **2018**, *8*, 1702463.

[16] Wu, D. Z.; Zhuang, Y. C.; Wang, F.; Yang, Y.; Zeng, J.; Zhao, J. B. High-rate performance magnesium batteries achieved by direct growth of honeycomb-like V_2O_5 electrodes with rich oxygen vacancies. *Nano Res.* **2023**, *16*, 4880–4887.

[17] Boruah, B. D.; Mathieson, A.; Wen, B.; Feldmann, S.; Dose, W. M.; De Volder, M. Photo-rechargeable zinc-ion batteries. *Energy Environ. Sci.* **2020**, *13*, 2414–2421.

[18] Li, Y. K.; Huang, Z. M.; Kalambate, P. K.; Zhong, Y.; Huang, Z. M.; Xie, M. L.; Shen, Y.; Huang, Y. H. V_2O_5 nanopaper as a cathode material with high capacity and long cycle life for rechargeable aqueous zinc-ion battery. *Nano Energy* **2019**, *60*, 752–759.

[19] Boruah, B. D.; Mathieson, A.; Park, S. K.; Zhang, X.; Wen, B.; Tan, L. F.; Boies, A.; De Volder, M. Vanadium dioxide cathodes for high-rate photo-rechargeable zinc-ion batteries. *Adv. Energy Mater.* **2021**, *11*, 2100115.

[20] Boruah, B. D.; Wen, B.; De Volder, M. Molybdenum disulfide-zinc oxide photocathodes for photo-rechargeable zinc-ion batteries. *ACS Nano* **2021**, *15*, 16616–16624.

[21] Liu, F.; Chen, Z. X.; Fang, G. Z.; Wang, Z. Q.; Cai, Y. S.; Tang, B. Y.; Zhou, J.; Liang, S. Q. V_2O_5 nanospheres with mixed vanadium valences as high electrochemically active aqueous zinc-ion battery cathode. *Nano-Micro Lett.* **2019**, *11*, 25.

[22] Chen, H. D.; Huang, J. J.; Tian, S. H.; Liu, L.; Qin, T. F.; Song, L.; Liu, Y. P.; Zhang, Y. N.; Wu, X. G.; Lei, S. L. et al. Interlayer modification of pseudocapacitive vanadium oxide and $Zn(H_2O)_n^{2+}$ migration regulation for ultrahigh rate and durable aqueous zinc-ion batteries. *Adv. Sci.* **2021**, *8*, 2004924.

[23] Tian, M.; Liu, C. F.; Zheng, J. Q.; Jia, X. X.; Jahrman, E. P.; Seidler, G. T.; Long, D. H.; Atif, M.; Alsalhi, M.; Cao, G. Z. Structural engineering of hydrated vanadium oxide cathode by K^+ incorporation for high-capacity and long-cycling aqueous zinc ion batteries. *Energy Storage Mater.* **2020**, *29*, 9–16.

Yinan Lu earned her Bachelor's and Master's degrees in Materials Science and Engineering from Nanyang Technological University. Currently, she is a PhD candidate at University College London, under the supervision of Assistant Professor Buddha Deka Boruah and Prof. Ivan P. Parkin. Her research focuses on enhancing the electrochemical performance of vanadium-based cathode materials utilised in both lithium-ion and zinc-ion batteries.

Tianlei Wang received his Bachelor's degree in Chemistry from Lanzhou University, followed by a Master's degree in Chemical Engineering from Tianjin University. He is currently a PhD candidate in the Department of Chemistry at University College London under the supervision of Prof. Ivan P. Parkin. His primary research focuses on electrocatalysts for the oxygen reduction reaction.

Nibagani Naresh currently serves as a postdoctoral research fellow, working under the guidance of Assistant Professor Dr. Buddha Deka Boruah at the Institute for Materials Discovery, University College London. He earned his Ph.D. from Pondicherry University, India, in 2020, and has previously held a postdoctoral position at Gyeongsang National University, South Korea. His research is centered on advancing lithium-ion batteries, aqueous zinc-ion batteries, and micro-batteries.

Ivan P. Parkin is an inorganic materials chemist, who became Faculty Dean of Mathematical & Physical Sciences in October 2016. Prior to his appointment as Dean, he was Head of Department for UCL Chemistry for 6 ½ years. Ivan is a fellow of the Royal Society of Chemistry, a fellow of the Institute of Mining Materials and Metallergy and a member of Academia Europaea. He is a Chartered Chemist and Chartered Scientist. His group has published 1000 publications and he has been awarded 9 medals and prizes from learned societies. He is in the world's top 6000 citated authors for 2023 by Clarivate and has an H- index of 110.

Buddha Deka Boruah earned his B.Sc. in Physics from Cotton College, Assam, India, in 2011. Subsequently, he completed his M.Sc. degree in Physics at the Indian Institute of Technology (IIT) Guwahati, India, in 2013. Following that, he pursued his M.S. in Engineering-Ph.D. at the Indian Institute of Science (IISc), Bangalore, India, culminating in 2018. In 2018, he was awarded The Royal Society - Newton International Fellowship (NIF) and joined the Department of Engineering at the University of Cambridge, UK, as a postdoctoral research fellow. Later, in 2022, he established his research group at University College London. His research endeavors primarily revolve around micro-batteries, aqueous rechargeable batteries, and photo-rechargeable batteries.